



# Effect of dark matter halo on transonic accretion flow around a galactic black hole

Subhankar Patra \* and Bibhas Ranjan Majhi †

*Department of Physics, Indian Institute of Technology Guwahati, Guwahati 781039, Assam, India*

(Dated: January 14, 2025)

We investigate the transonic accretion flow in the spacetime of a supermassive black hole (BH) coupled to an anisotropic dark matter fluid, as proposed by Cardoso *et al.* We essentially compare the accretion properties of the Cardoso BH with those of an isolated Schwarzschild BH. The Cardoso BH is described by the halo mass ( $M_H$ ) and its characteristic length scale ( $a_0$ ). Various classes of accretion solution topologies (e.g., O, A, and I-types), including the shock solutions, are obtained by solving the dynamical equations of the flow in a fully general relativistic framework. We find that the accretion solutions are substantially influenced by the halo parameters ( $M_H, a_0$ ) when the dark matter distribution is concentrated near the BH horizon. In this context, we also observe that various shock properties, such as the shock radius, flow density compression, and temperature compression across the shock fronts, are potentially affected by the dark halo. Interestingly, the existing shock parameter space, defined by the flow angular momentum and energy, is largely reduced for higher halo compactness compared to that of the Schwarzschild BH. Furthermore, different observational signatures of the accretion disc, like the spectral energy distribution (SED), slope of the SED, and bolometric luminosity, are found to exhibit strong deviations from the known results in the usual Schwarzschild BH model. These unique features offer a possible valuable tool for characterizing the presence or absence of a dark matter halo around a galactic BH.

Keywords: accretion; astrophysical fluid dynamics; astrophysical black holes; active galactic nuclei

## I. INTRODUCTION

Astrophysical sources such as active galactic nuclei (AGN) and black hole X-ray binaries (BH-XRBs) are powered by the accretion of matter and emit electromagnetic radiation across all frequency domains [1, 2]. Over timescales of a few days to months, their spectral state changes from the low-hard state (LHS) to the high-soft state (HSS) through several intermediate states [3, 4]. To understand their spectral characteristics, numerous accretion models have been proposed in the literature, depending on different physical conditions [5, 6, and references therein]. Indeed, all those analyses provide essential properties of the accretion disk, such as mass accretion and outflow rates, size of the post-shock corona (PSC), disk inclination angle, quasi-periodic oscillation (QPO) frequency, photon index, etc [4, 7–16]. Also, these studies offer information about the central black holes, i.e., their mass and spin [7, 9, 12, 13, 17, 18].

A number of scenarios support the presence of a dark matter halo around the supermassive black holes in AGNs [19]. Since dark matter interacts weakly, possibly through the weak nuclear force, its exact properties still remain unknown [20]. However, it can interact gravitationally with the normal matter, thereby altering the

geometry of spacetime. To know how dark matter influences the gravitational wave (GW) and electromagnetic (EM) observations of black holes, a proper spacetime manifold is required. Several attempts have been made to construct such a BH spacetime at the Newtonian level. However, going beyond these approximate models, Cardoso *et al.* [21] proposed an exact analytical solution within Einstein's general relativity (GR), which represents a supermassive BH spacetime minimally coupled to a dark matter fluid with anisotropic pressure and Hernquist density profile. In this fully GR approach, few other BH metrics are modeled by considering different density profiles of the dark matter (e.g., King, Einasto, Jaffe, Burkert, Navarro–Frenk–White, Moore, Taylor–Silk profiles, etc.) [22–36]. Although various properties of spacetime and phenomenology have been investigated to observe the influence of dark halos [37–50], their effect on transonic matter accretion [51–53] onto black holes has not been studied. In this work, we aim to explore how the presence of a dark matter halo can be perceived through different transonic accretion properties. In this regard, we would like to concentrate on the Cardoso BH model only because, for most of the galaxies, it is consistent with the observed rotation curves and other dynamical properties as well. Needless to mention that the choice of the dark matter profile depends on the specific context and the kind of galaxy or dark matter halo being modeled.

The Cardoso BH is described by two independent pa-

---

\* [psubhankar@iitg.ac.in](mailto:psubhankar@iitg.ac.in)

† [bibhas.majhi@iitg.ac.in](mailto:bibhas.majhi@iitg.ac.in)

rameters: halo mass ( $M_{\text{H}}$ ) and characteristic length scale ( $a_0$ ). Recently, interest has grown in testing the Cardoso model on the rich astrophysical environments of the black holes, such as accretion discs, photon rings, etc. For example, in [21], the authors investigated the effect of dark halo on GWs emission and propagation. The influence of dark matter components on the properties of EM radiations, like the quasi-normal modes, perturbations, scatterings, etc., has been studied in [54]. The epicyclic oscillatory motion of the test particles and its application to the observed QPOs in AGN spectra were explored in [55]. The investigation of the tidal forces and geodesic deviation motion due to a dark matter halo has been reported in [56]. The evolution of the extreme mass ratio inspiral in a galactic black hole spacetime within the dark halo is analyzed in [40]. In presence of a dark halo, the black hole shadow is studied in [41], where the authors constrained the halo parameters ( $M_{\text{H}}$ ,  $a_0$ ) using the Event Horizon Telescope (EHT) collaborations shadow data for the supermassive black holes M87\* and SgrA\*. The energy spectrum and fluxes of the orbiting particles are examined in [44] based on the Novikov-Thorne accretion model. The effect of a dark matter halo on the motion of spinning particles was investigated in [46]. The analysis of quasi-normal modes of a galactic black hole in a dark matter halo has been explored in [49].

For black hole accretion, a key feature is that the flow must satisfy the inner boundary conditions at the event horizon. These conditions imply that the angular momentum of the flow should be sub-Keplerian near the horizon and cross the horizon at the speed of light. In that way, the flow motion must be transonic in nature, where the flow speed changes from subsonic to supersonic values [57–67, and references therein]. In the last few decades, the study of transonic accretion models has largely increased, as these models explain many observational signatures of the accretion disk near the black hole, such as hard power-law spectra, QPOs, and bipolar jets in the PSC, etc [9, 66, 68–70].

As we have seen, many strong gravity signatures have been analyzed in the Cardoso BH model, and some great results have been revealed. But, till now, to the best of our knowledge, nobody has reported the transonic accretion flows around the Cardoso BH. Such deficiency in the literature motivates us to serve the present work. We explore the transonic accretion solutions and associated observational signatures (e.g., luminosity distributions, spectrum slope, bolometric disc luminosity, etc.) in presence and absence of the shock waves in background of the Cardoso BH metric. Our results indicate that the halo parameters ( $M_{\text{H}}$ ,  $a_0$ ) potentially affect the accretion

disc properties when the dark matter concentrates close to the black hole. However, for low compactness, these properties deviate insignificantly from the Schwarzschild BH model. In the high compactness regime, we compare the outcomes of the Cardoso BH model with those for the vacuum Schwarzschild BH model. We show that the high compactness of the halo largely modulates a given accretion solution topology (e.g., O, A, I-types, and shock solutions) with respect to the usual Schwarzschild BH spacetime. Additionally, the high compactness confines the shock solutions to a narrower range of flow angular momentum and energy than in the case of the Schwarzschild BH, leaving mostly I-type solutions in the system. Such effects change the flow temperature in the disc significantly. Consequently, the disc luminosity and spectrum shape of the emitted radiation are varied substantially compared to the results in the Schwarzschild BH model. These observational features may help to sense the existence of a dark matter halo around a galactic black hole.

The outlines of this paper are as follows. In Section II, we introduce the black hole metric with a dark matter halo. Section III presents the governing flow equations for the accretion disc in a static and asymmetric spacetime. In Section IV A, we discuss the methodology used to find transonic accretion solutions and see the effect of the dark halo on solution topologies and their physical properties as well. In Section IV B, we analyze the shock-induced accretion solutions and explore various shock properties as a function of halo compactness. The available parameter space for shocks and their modifications with halo parameters have been depicted in Section IV C. Finally, in Section V, we conclude our results.

## II. GEOMETRY OF GALACTIC BLACK HOLE WITH DARK MATTER HALO

In this section, we introduce the background spacetime, which has been used in our analysis, and discuss its properties. In [21], the authors provided an exact analytical solution of Einstein’s equations for describing a supermassive BH immersed in a dark matter halo. To do that, they follow the Einstein construction, where the anisotropic matter has tangential pressure only. They generalized the Einstein cluster, a technique to construct a stationary system of many gravitating masses, by including a black hole at the center of a dark matter distribution. Accordingly, the general relativistic geometry

of such configuration is found to be [21],

$$ds^2 = -f(r)dt^2 + \frac{dr^2}{1 - 2m(r)/r} + r^2 d\Omega^2, \quad (1)$$

where

$$d\Omega^2 = d\theta^2 + \sin^2\theta d\phi^2. \quad (2)$$

The mass function  $m(r)$  is chosen as,

$$m(r) = M_{\text{BH}} + \frac{M_{\text{H}}r^2}{(r + a_0)^2} \left(1 - \frac{2M_{\text{BH}}}{r}\right)^2, \quad (3)$$

where  $M_{\text{BH}}$  is the mass of the central black hole,  $M_{\text{H}}$  is the mass of dark matter halo, and  $a_0$  is the typical length scale that governs the size of the dark matter halo. The specialty of choosing such a mass profile is that it corresponds to the black hole mass  $M_{\text{BH}}$  at small distances. On the other hand, at large scales, it describes the Hernquist density profile as,

$$\rho_0(r) = \frac{M_{\text{H}}a_0}{2\pi r(r + a_0)^3}. \quad (4)$$

Using the mass profile (3) and imposing the asymptotic flatness condition (i.e.,  $f \rightarrow 1$  at  $r \rightarrow \infty$ ), the radial function is obtained from the Einstein's equation as,

$$f(r) = \left(1 - \frac{2M_{\text{BH}}}{r}\right) e^{\gamma(r)}, \quad (5)$$

where

$$\gamma(r) = -\pi\sqrt{\frac{M_{\text{H}}}{\xi}} + 2\sqrt{\frac{M_{\text{H}}}{\xi}} \arctan\left(\frac{r + a_0 - M_{\text{H}}}{\sqrt{M_{\text{H}}\xi}}\right), \quad (6)$$

$$\xi = 2a_0 - M_{\text{H}} + 4M_{\text{BH}}. \quad (7)$$

The matter density ( $\rho_0$ ) and tangential pressure ( $P_t$ ) corresponding to the solution (5) are obtained as,

$$\rho_0(r) = \frac{1}{4\pi r^2} \frac{dm(r)}{dr} = \frac{2M_{\text{H}}(a_0 + 2M_{\text{BH}})(1 - 2M_{\text{BH}}/r)}{r(r + a_0)^3}, \quad (8)$$

$$P_t(r) = \frac{m(r)\rho_0}{2[r - 2m(r)]}. \quad (9)$$

The black hole solution described by Eq. (1) has a regular event horizon at  $r = r_{\text{H}} = 2M_{\text{BH}}$  and the curvature singularity at  $r = 0$ . The ADM mass of the spacetime is given by  $M_{\text{ADM}} = M_{\text{BH}} + M_{\text{H}}$ . It is noted that at the horizon,  $\rho_0$  vanishes, while  $P_t$  remains regular. Moreover, the dark matter fluid satisfies both the weak and strong energy conditions everywhere outside the horizon, as both  $\rho_0$  and  $P_t$  are always positive. However, near

$r_{\text{H}}$ ,  $P_t/\rho_0$  diverges because  $\rho_0$  becomes very small. As a result, the dominant energy condition is violated in this region. Nevertheless, this does not affect the spacetime dynamics as the near-horizon region is nearly empty due to the small values of  $\rho_0$  and  $P_t$ . In this dark matter model, the condition  $M_{\text{BH}} \ll M_{\text{H}} \ll a_0$  defines the astrophysical setup. To quantify the compactness of the halo, a parameter  $C = M_{\text{H}}/a_0$ , known as the compactness parameter, is introduced. In the work [26], this parameter is constrained to  $C \leq 10^{-4}$  based on the galaxy observations. However, it can be treated as a free parameter when specifically analyzing the black hole environments, such as the GWs propagation deep in galactic cores. Thereafter, Xavier et al. [41] analyzed the light rings, another rich black hole environment, and reported that  $C$  values greater than unity do not align with the shadow data from the EHT collaborations. In our study, we consider  $C$  values below the limit provided by the shadow observations in [41] as we focus on the accretion process, which is also a potential candidate for black hole environments. It is expected that  $C$  could be constrained more precisely by future high-precision observations.

### III. MODEL EQUATIONS GOVERNING ACCRETION DISC

The dynamical equations governing the accretion flow in the spacetime (1) have been developed in this section. We model the hydrodynamics of accretion flow within a complete general relativistic setting [71]. We assume that the motion of an ideal fluid is confined to the equatorial plane (i.e.,  $\theta = \pi/2$ ) of the central black hole, meaning the flow has no transverse motion (i.e.,  $u^\theta = 0$ , where  $u^\theta$  is  $\theta$  component of the four-velocity  $u^k$ ). Also, we have  $\partial_\theta Q = 0$ , where  $Q$  is any flow parameter (e.g., mass density, pressure, and temperature, etc.). Moreover, the fluid is steady (i.e.,  $\partial_t Q = 0$ ) and obeys the azimuthal symmetry of the spacetime (i.e.,  $\partial_\phi Q = 0$ ). To simplify the fluid motion to one dimension (radial motion only), we adopt a co-rotating frame (CRF), which rotates with the same angular velocity as the fluid. In this work, we choose a unit system such that  $G = M_{\text{BH}} = c = 1$ , where  $G$  is the gravitational constant and  $c$  is the speed of light. Such a choice makes all the physical quantities dimensionless. Under these assumptions, the radial momentum equation can be written as [59],

$$\gamma_v^2 v \frac{dv}{dr} + \frac{1}{e + p} \frac{dp}{dr} + \left(\frac{d\Phi^{\text{eff}}}{dr}\right)_\lambda = 0, \quad (10)$$

where  $\gamma_v$  is the Lorentz-factor corresponding to the radial component of the physical three-velocity ( $v$ ) in the CRF,

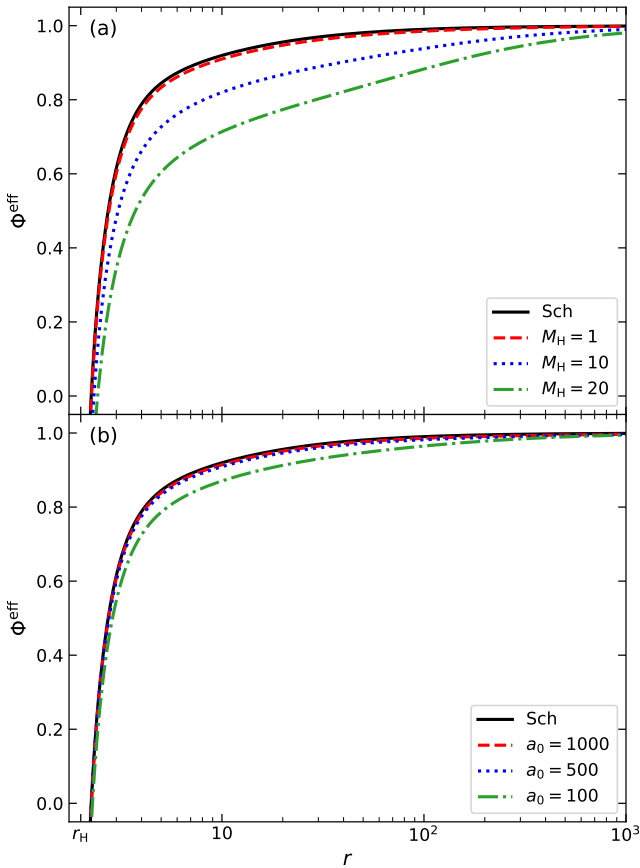


FIG. 1. Plot of effective potential ( $\Phi^{\text{eff}}$ ) as a function of radial distance ( $r$ ) for halo masses  $M_H = 1, 10,$  and  $20$  with a given length scale  $a_0 = 100$  (panel (a)), and for  $a_0 = 1000, 500,$  and  $100$  with  $M_H = 5$  (panel (b)). The solid (black) lines are used for the Schwarzschild BH. In this figure, the flow angular momentum is taken as  $\lambda = 2.75$ . See the text for details.

$e$  is the total internal energy density,  $p$  is the isotropic fluid pressure,  $\Phi^{\text{eff}}$  is the effective potential of the system, and  $\lambda$  ( $= -u_\phi/u_t$ , where  $u_\phi$  and  $u_t$  are the  $\phi$  and  $t$  components of  $u_k$ ) is the specific angular momentum of fluid. Note that for accretion,  $v$  is a negative quantity. The expression of  $\Phi^{\text{eff}}$  is obtained in terms flow parameter  $\lambda$  and spacetime parameters ( $M_H, a_0$ ) as,

$$\Phi^{\text{eff}} = 1 + \frac{1}{2} \ln(\Phi), \quad \Phi = \frac{r^2(r-2)e^{\gamma(r)}}{r^3 - \lambda^2(r-2)e^{\gamma(r)}}. \quad (11)$$

In Fig. 1, we show the variation of  $\Phi^{\text{eff}}$  with  $r$  for different values of  $M_H$  and  $a_0$ , while keeping fixed  $\lambda = 2.75$ . In panel (a), we set  $a_0 = 100$  and use the dashed (red), dotted (blue), and dash-dotted (green) curves to present the results for  $M_H = 1, 10,$  and  $20$ , respectively. Similarly, in panel (b), the profiles of  $\Phi^{\text{eff}}$  are plotted as a function of  $a_0$  for a fixed  $M_H = 5$ . The dashed (red), dotted (blue), and dash-dotted (green) curves correspond to  $a_0 = 1000,$

$500,$  and  $100,$  respectively. Here, the solid (black) curves represent the results for the Schwarzschild BH model with the absence of dark matter halo. From Fig. 1, it is evident that  $\Phi^{\text{eff}}$  undergoes significant changes as both  $M_H$  and  $a_0$  are increased.

In steady state, mass accretion rate ( $\dot{M}$ ) is usually taken as a constant of motion (i.e.,  $d\dot{M}/dr = 0$ ). Integrating the conservation equation of mass flux (i.e.,  $\nabla_k(\rho u^k) = 0$ ,  $\rho$  is the mass density of flow), we get the expression of  $\dot{M}$  as,

$$\dot{M} = -4\pi\rho H v \gamma_v \sqrt{r(r-2)} e^{\gamma(r)} = \text{constant}, \quad (12)$$

where  $H$  is the half-thickness of the disc. Considering the hydrostatic equilibrium along the vertical direction of the disc,  $H$  is calculated as [72–74],

$$H = \sqrt{\frac{pr^3}{\rho F}}, \quad (13)$$

where  $F = 1/(1 - \Omega\lambda)$ . The angular velocity ( $\Omega$ ) of the flow is given by,

$$\Omega = \frac{u^\phi}{u^t} = \frac{\lambda(r-2)e^{\gamma(r)}}{r^3}. \quad (14)$$

In our model, the other constant of motions can be found from the present spacetime symmetries. We find two conserved quantities along the streamlines of the flow as (a) Bernoulli constant:  $E = -(e + p)u_t/\rho$  (from time-translation symmetry), and (b) bulk angular momentum:  $\mathcal{L} = (e + p)u_\phi/\rho$  (from azimuthal symmetry). Therefore,  $\lambda$  ( $= -\mathcal{L}/E$ ) appears to be another constant of motion.

We consider a relativistic equation of state as proposed in [75], where a variable adiabatic index  $\Gamma$  is used instead of assuming a constant value. Following that work, the thermodynamic variables  $e$  and  $p$  can be found as,

$$e = \frac{\rho f}{1 + m_p/m_e}, \quad p = \frac{2\rho\Theta}{1 + m_p/m_e}, \quad (15)$$

where  $m_p$  is the proton mass and  $m_e$  is the electron mass. The quantity  $f$  is expressed in term of dimensionless temperature  $\Theta$  ( $= k_B T/(m_e c^2)$ ,  $k_B$  is the Boltzmann constant and  $T$  is the flow temperature in Kelvin) as,

$$f = 1 + \frac{m_p}{m_e} + \Theta \left[ \frac{9\Theta + 3}{3\Theta + 2} + \frac{9\Theta + 3m_p/m_e}{3\Theta + 2m_p/m_e} \right]. \quad (16)$$

After solving the equation  $d\dot{M}/dr = 0$  using Eqs. (12), (13), and (15), the temperature gradient of the flow is obtained as,

$$\frac{d\Theta}{dr} = -\frac{2\Theta}{(df/d\Theta) + 1} \left( \frac{\gamma_v^2}{v} \frac{dv}{dr} + N_{11} + N_{12} \right), \quad (17)$$

with

$$N_{11} = \frac{3}{2r} + \frac{r-1}{r(r-2)} - \frac{1}{2F} \frac{dF}{dr}, \quad N_{12} = \frac{1}{2} \frac{d\gamma}{dr}. \quad (18)$$

As  $\dot{M}$  is very small for the context of supermassive black hole accretion [6, 76], we neglect the radiative cooling mechanism in the energy equation (first law of thermodynamics). Therefore, it is obtained as,

$$\frac{e+p}{\rho} \frac{d\rho}{dr} - \frac{de}{dr} = 0. \quad (19)$$

The expression of  $\rho$  is calculated by integrating Eq. (19) as,

$$\rho = \mathcal{K} e^\chi \Theta^{3/2} (3\Theta + 2)^{3/4} (3\Theta + 2m_p/m_e)^{3/4}, \quad (20)$$

where  $\mathcal{K}$  refers the entropy constant and  $\chi = (f - 1 - m_p/m_e)/(2\Theta)$ . From Eq. (19), it is evident that the flow is locally adiabatic, which implies constant entropy content. Following the works of [58, 77], the entropy accretion rate of the flow is found to be,

$$\dot{\mathcal{M}} = \frac{\dot{M}}{4\pi\mathcal{K}} = -v\gamma_v H \sqrt{r(r-2)e^{\gamma(r)}} \times e^\chi \Theta^{3/2} (3\Theta + 2)^{3/4} (3\Theta + 2m_p/m_e)^{3/4}. \quad (21)$$

To obtain the radial velocity gradient, we simultaneously solve Eqs. (10), (15), (17) and (19), which leads to the result,

$$\frac{dv}{dr} = \frac{\mathcal{N}}{\mathcal{D}}, \quad (22)$$

The expressions of numerator ( $\mathcal{N}$ ) and denominator ( $\mathcal{D}$ ) of the above equation are found to be,

$$\mathcal{N} = \frac{2C_s^2}{\Gamma + 1} (N_{11} + N_{12}) - \frac{d\Phi^{\text{eff}}}{dr}, \quad (23)$$

$$\mathcal{D} = \gamma_v^2 \left[ v - \frac{2C_s^2}{(\Gamma + 1)v} \right], \quad (24)$$

where  $C_s$  ( $= \Gamma p/(e+p)$ ) is the adiabatic sound speed with  $\Gamma = 1 + 2/(df/d\Theta)$ .

We consider the emission of thermal bremsstrahlung radiation from the accretion disk. Since the disk medium is optically thin for the hot accretion flow (HAF) [6, 64], bremsstrahlung radiation can escape from the disk without being absorbed [64]. We assume a completely ionized hydrogen plasma (atomic number  $Z = 1$ ), where the number densities of electrons and ions are the same, i.e.,  $n_e = n_p \approx \rho/m_p$ . Moreover, we use an approximate expression for the free-free emission coefficient, as proposed

by Novikov and Thorne [78], given by,

$$\mathcal{E}_{\nu_e}^{\text{ff}} = 6.8 \times 10^{-38} (\rho/m_p)^2 T_e^{-1/2} (1 + 4.4 \times 10^{-10} T_e) \times \exp\left(-\frac{h\nu_e}{k_B T_e}\right) \bar{g}_{\text{ff}} \text{ erg s}^{-1} \text{ cm}^{-3} \text{ Hz}^{-1}, \quad (25)$$

where  $h$  is the Planck constant,  $T_e$  is the electron temperature (scaled as  $T_e = T/10$  [76]),  $\nu_e$  is the emission frequency, and  $\bar{g}_{\text{ff}}$  is the thermally-averaged Gaunt factor (which includes quantum mechanical correction). In our analysis, we take  $\bar{g}_{\text{ff}} = 1.2$  [76]. The second term in Eq. (25) accounts for both electron-electron emission and relativistic corrections. It is important to note that for HAF, their effectiveness is significant [64].

For an observer at spatial infinity, the emission frequency is redshifted due to the strong gravitational potential of the central black hole, as well as the rotation of the disc. For simplicity, we neglect any light-bending effects on the emitted radiation. Additionally, the velocity distribution of the electrons is assumed to follow the standard Maxwell's prescription. Under these assumptions, the red-shift factor  $(1+z)$  is found to be [63, 79, 80],

$$1+z = \frac{\nu_e}{\nu_o} = u^t \left( 1 + \frac{r\Omega}{c} \sin\theta_0 \sin\phi \right), \quad (26)$$

with

$$u^t = \gamma_v \sqrt{\frac{r}{(1-\Omega\lambda)(r-2)e^{\gamma(r)}}}. \quad (27)$$

Here,  $\nu_o$  is the observed frequency and  $\theta_0$  is the inclination angle of the accretion disc with respect to the distant observer frame. We take  $\theta_0 = 45^\circ$  for the purpose of illustration. Using Eqs. (25) and (26), we get the monochromatic disc luminosity measured by an observer at infinity as,

$$L_{\nu_o} = 2 \int_{r_{\text{H}}}^{r_{\text{edge}}} \int_0^{2\pi} \mathcal{E}_{\nu_o}^{\text{ff}} H r dr d\phi \text{ erg s}^{-1} \text{ Hz}^{-1}, \quad (28)$$

where  $r_{\text{H}}$  is taken as the inner edge of the disc. The outer edge of the disc is assumed to be at  $r_{\text{edge}} = 1000$ .

Finally, integrating Eq. (28) over all frequency domains, we calculate the bolometric disc luminosity as,

$$L = \int_0^\infty L_{\nu_o} d\nu_o \text{ erg s}^{-1}. \quad (29)$$

The above equations are useful for finding the accretion solutions and their corresponding disc properties, such as temperature profile, disc luminosity, and spectral energy distribution, etc. Note that when we set halo mass  $M_{\text{H}} = 0$  in these equations, we can recover the flow equations in the usual Schwarzschild BH spacetime. A detailed discussion of the accretion properties around the galactic black hole metric (1) is provided in Section IV.



## IV. RESULTS

### A. Transonic accretion solutions

This section explores the transonic accretion solutions, where the flow must pass through at least one critical point [51, 52]. Critical points ( $r_c$ ) are such radial coordinates where the velocity gradient  $dv/dr$  (see Eq. (22)) takes the form “0/0”. Therefore, the necessary conditions for finding the critical points are  $\mathcal{N} = \mathcal{D} = 0$ . Note that flow may possess single or multiple critical points depending on the global constants  $\lambda$ ,  $E$ ,  $M_H$ , and  $a_0$ . However, the multiple critical points scenario is of special interest for generating shocks [61, 63–66, 70, 81], which has been extensively discussed in Section IV B. The critical points that are formed close to the horizon are called inner critical points ( $r_{in}$ ), and those formed far away from the horizon are called the outer critical points ( $r_{out}$ ). As  $(dv/dr)_{r_c}$  takes an indeterminate form, we use the l’Hôpital’s rule to Eq. (22) for finding the finite values of  $dv/dr$ . Usually,  $(dv/dr)_{r_c}$  have two values. Depending on them, critical points are classified into three categories — (a) saddle-type:  $(dv/dr)_{r_c}$  values are real with opposite sign; (b) nodal-type:  $(dv/dr)_{r_c}$  values are real with the same sign; and (c) spiral-type: both values of  $(dv/dr)_{r_c}$  are imaginary. The positive value of  $dv/dr$  corresponds to an accretion solution, and the negative value of  $dv/dr$  yields a wind solution. Therefore, out of three types of critical points, only the saddle-type critical points (hereafter called critical points) are physically acceptable. In this work, we focus on accretion solutions that only pass through saddle-type critical points, excluding any analysis of wind solutions. To find the accretion solutions, we first calculate  $r_c$  and its corresponding flow variables  $\Theta_c$  and  $v_c$  for a given set of global constants ( $\lambda, E, M_H, a_0$ ). Using those results as an initial boundary condition, we then numerically solve the differential Eqs. (17) and (22) from  $r_c$  to  $r_{edge}$  and also from  $r_c$  to  $r_H$ . Finally, combining the two segments of the solution, we obtain a complete accretion solution.

Following the above methodology, we find the transonic accretion solutions for different sets of input parameters. The obtained results are presented in Fig. 2a, where the Mach number ( $M = |v|/C_s$ ) is plotted as a function of the radial distance ( $r$ ). Here, the flow parameters are chosen as  $\lambda = 2.75$  and  $E = 1.0025$ . We fix the length scale at  $a_0 = 500$  and vary the halo mass  $M_H$ . The solid (black) curve corresponds to the Schwarzschild BH without dark matter halo (i.e.,  $M_H = 0$ ), while the dashed (red), dotted (blue), dash-dotted (green), and long-dashed (magenta) curves represent the results for

the Cardoso BH with  $M_H = 1, 5, 10$ , and  $50$ , respectively. In all cases, the solutions extend from  $r_{edge}$  to  $r_H$ , which are characteristic of open or global accretion solutions. For the Schwarzschild BH model, the solution is found to be pass through the outer critical point at  $r_{out} = 85.0892$ . In presence of the dark matter halo with  $M_H = 1$ , the solution again passes through  $r_{out}$  but with a significantly decreased value of  $r_{out} = 47.2185$ . Accretion solutions that pass through  $r_{out}$  are referred to as O-type solution topology. When  $M_H$  is increased to 5, the accretion solution now passes through the inner critical point at  $r_{in} = 7.39$ . Such accretion solutions that pass through  $r_{in}$  are known as I-type solution topology. For a further increase in the halo mass  $M_H = 10$ , the solution topology remains I-type, with  $r_{in} = 6.5138$ . When the halo mass is increased even more to  $M_H = 50$ , the solution topology continues to be I-type, but now the inner critical point moves closer to the horizon, with  $r_{in} = 4.8793$ . Similarly, in Fig. 2b, we present the global accretion solutions for a fixed halo mass  $M_H = 10$  with varying length scale  $a_0$ . In this case, we choose the same set of flow parameters ( $\lambda, E$ ) as used in Fig. 2a. The obtained results are shown using the dashed (red), dotted (blue), dash-dotted (green), and long-dashed (magenta) lines for  $a_0 = 10^5, 10^4, 10^3$ , and  $10^2$ , respectively. Here, the solid (black) curve corresponds to the usual Schwarzschild case, as shown in Fig. 2a, and has been included again for the comparison with dark matter model. For Cardoso BH with large values of  $a_0$ , such as  $a_0 = 10^5$  and  $10^4$ , the solutions remain O-type, similar to the Schwarzschild BH, with outer critical points at  $r_{out} = 81.6338$  and  $58.5248$ , respectively. However, for smaller values of  $a_0$ , such as  $a_0 = 10^3$  and  $10^2$ , the solution topology changes to I-type, with  $r_{in}$  values continuously decreasing to 7.3628 and 4.9843, respectively.

The radial velocity profiles corresponding to the accretion solutions of panels (a) and (b) are shown in Figs. 2c-d, respectively. We observe that the flow velocity is minimal (i.e.,  $v \ll 1$ ) at the outer region of the disc. As the flow moves towards the black hole,  $v$  increases and eventually exceeds the local sound speed  $C_s$  after passing through the critical point  $r_c$ . Subsequently, the flow becomes supersonic and continues to move towards the horizon. Finally, at  $r_H$ ,  $v$  approaches the light speed  $c$ , satisfying the inner boundary condition of the transonic accretion model. In Figs. 2e-f, we present the profiles of the electron temperature  $T_e$  for the accretion solutions shown in Figs. 2a-b. In all cases,  $T_e$  increases as we move towards  $r_H$  from  $r_{edge}$ . We observe that the temperature distribution of the disk rises as  $r_c$  drifts toward the horizon. Also, the solutions associated with  $r_{in}$  exhibit

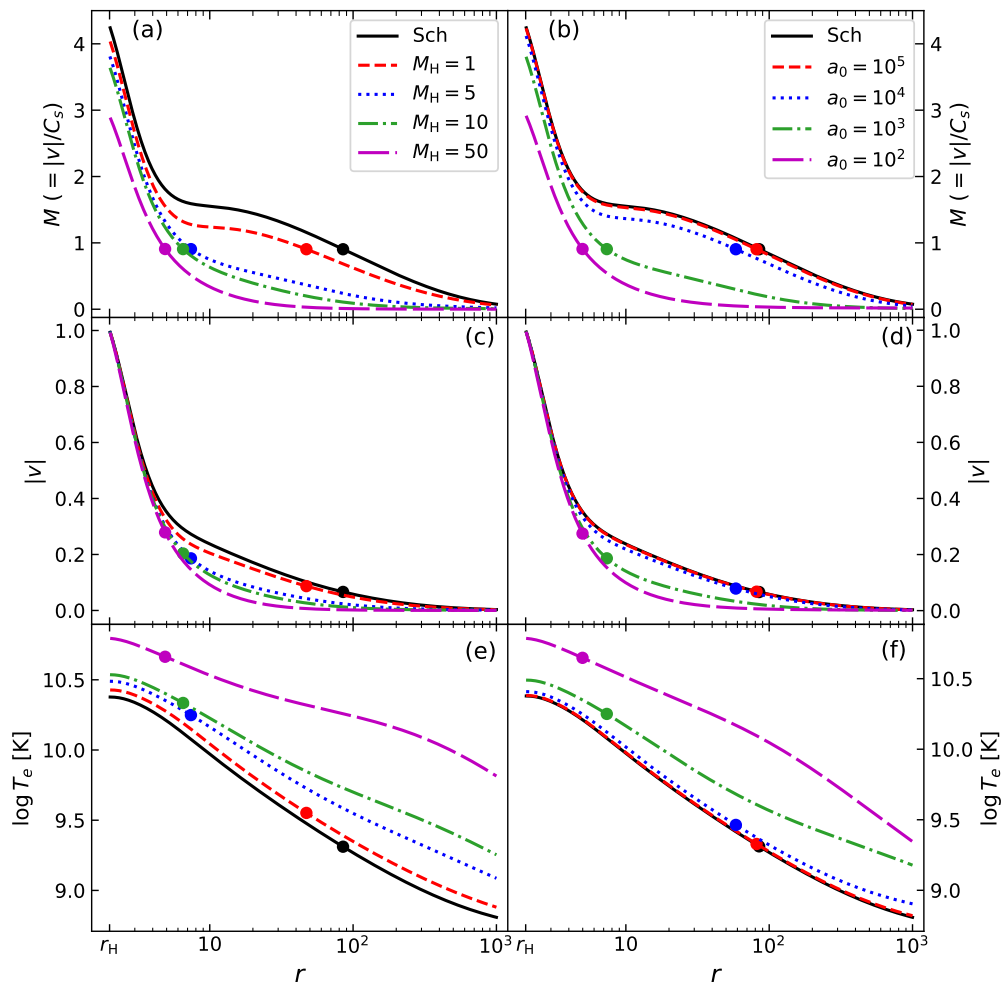


FIG. 2. Typical accretion solutions (i.e., Mach number ( $M = |v|/C_s$ ) versus radial distance ( $r$ ) plots) for halo masses  $M_H = 1, 5, 10,$  and  $50$  with length scale  $a_0 = 500$  (panel (a)), and for  $a_0 = 10^5, 10^4, 10^3,$  and  $10^2$  with  $M_H = 10$  (panel (b)). Panels (c) and (d) show the respective radial velocity ( $v$ ) profiles. The electron temperature ( $T_e$ ) profiles for panels (a) and (b) are presented in panels (e) and (f), respectively. In each panel, the solid (black) line corresponds to the Schwarzschild black hole without a dark matter halo ( $M_H = 0$ ). The critical points are marked by filled circles. In this figure, we choose  $\lambda = 2.75$  and  $E = 1.0025$ . See the text for details.

relatively higher  $T_e$  profiles compared to the solutions that pass through  $r_{\text{out}}$ . In Table I, we summarize the properties of the critical points related to the accretion solutions presented in Figs. 2a-b. This table highlights the changing behaviors of the accretion solutions and illustrates the potential shifting of the critical points as the halo compactness increases, specifically in terms of increasing  $M_H$  and decreasing  $a_0$ .

Next, we investigate the spectral properties of the accretion disc and examine how they are affected by the compactness of the dark matter halo. In this work, we consider a supermassive black hole with  $M_{\text{BH}} = 10^6 M_\odot$ , where  $M_\odot$  is the Solar mass. The mass accretion rate is taken to be very small as  $\dot{M} = 10^{-5} \dot{M}_{\text{Edd}}$ , where

$\dot{M}_{\text{Edd}} = 1.39 \times 10^{18} M_{\text{BH}}/M_\odot \text{ gm s}^{-1}$  is the Eddington mass accretion rate. We calculate the spectral energy distribution (SED) associated with the accretion solutions of Figs. 2a-b using Eq. (28). The obtained results are shown in the respective panels (a) and (b) of Fig. 3, where the variation of the quantity  $\nu_o L_{\nu_o}$  as a function of the observed frequency  $\nu_o$  is depicted. In all cases, the emitted radiation maximizes power at  $\nu_o \approx 10^{20}$  Hz. Also, the spectra exhibit a sharp cut-off around  $\nu_o \approx 10^{22}$  Hz ( $= k_B T_{e0}/h$ ), which corresponds to the disc inner edge electron temperature  $T_{e0} \approx 10^{11}$  K. We find that the SEDs for the Schwarzschild BH are lower than those for the Cardoso BH. This is because electron temperature across the entire disc in the Schwarzschild model is lower

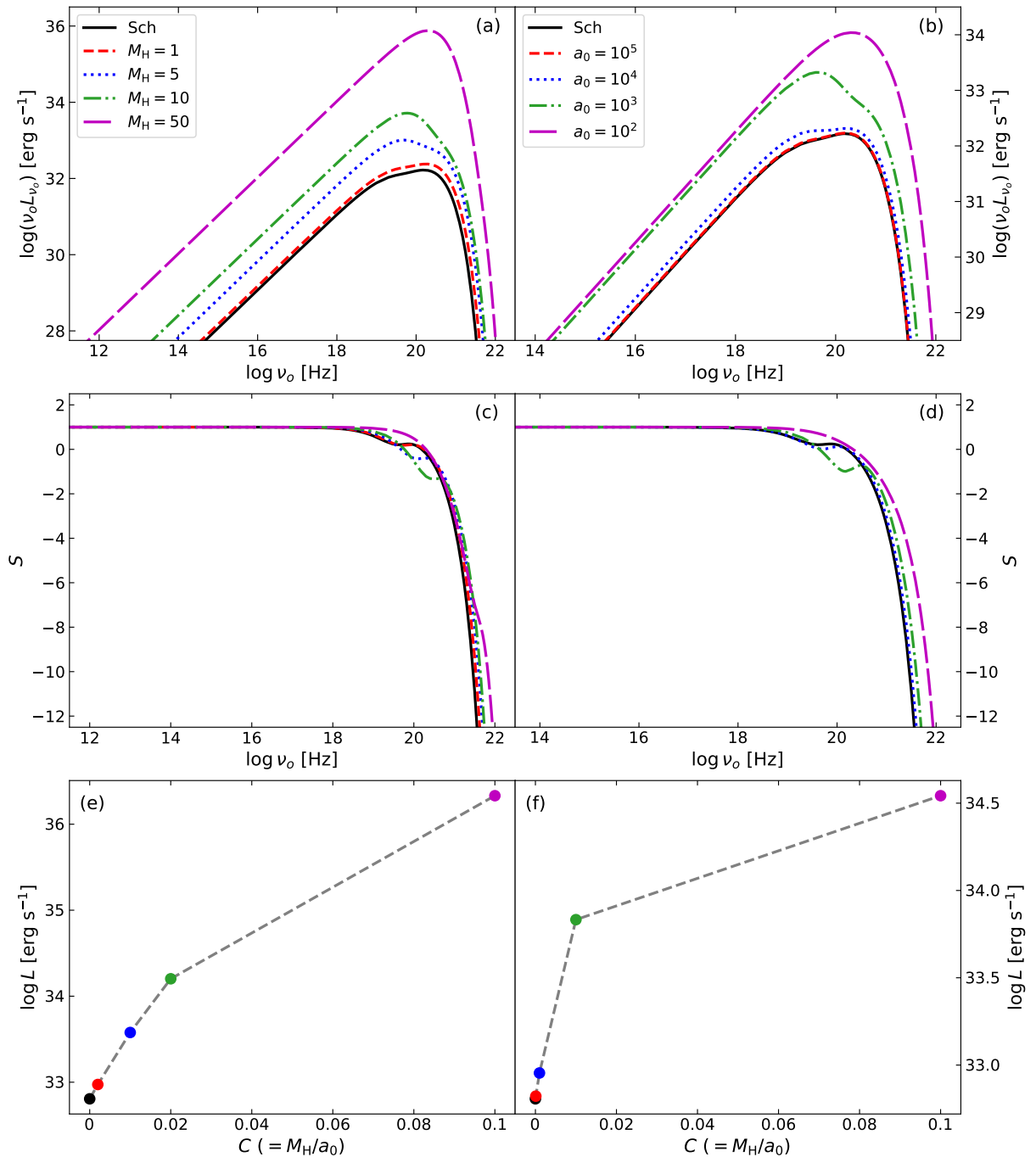


FIG. 3. Panels (a) and (b) represent the spectral energy distribution (i.e.,  $\nu_o L_{\nu_o}$  versus  $\nu_o$  curves) of the emitted radiation from the accretion disc for the accretion solutions shown in Fig. 2a and Fig. 2b, respectively. The slopes ( $S$ ) of the SED are presented in panels (c) and (d). The effect of halo compactness ( $C$ ) on the bolometric disc luminosity ( $L$ ) is depicted in panels (e) and (f). The filled circles represent the  $L$  values corresponding to the accretion solutions of Figs. 2a-b. Here, the input parameters are chosen as  $r_{\text{edge}} = 1000$ ,  $\lambda = 2.75$ ,  $E = 1.0025$ ,  $M_{\text{BH}} = 10^6 M_{\odot}$ , and  $\dot{M} = 10^{-5} \dot{M}_{\text{Edd}}$ . See the text for details.

compared to the Cardoso model (see Figs. 2e-f). Moreover, we observe that the SED increases with the rise in  $M_H$  and  $a_0$ , which is due to the corresponding increase in  $T_e$ , as shown in Figs. 2e-f. As the shape of the spectrum

begins to differ with increasing  $M_H$  and  $a_0$ , we explore the slopes of the luminosity spectrum to analyze these variations more quantitatively. For a log-log plot between



TABLE I. Dark matter halo mass ( $M_{\text{H}}$ ), halo length scale ( $a_0$ ), critical point locations ( $r_{\text{in}}, r_{\text{out}}$ ), critical point temperatures ( $T(r_{\text{in}}), T(r_{\text{out}})$ ), and topology types for the accretion solutions presented in Fig. 2.

$M_{\text{H}}$	$a_0$	$r_{\text{in}}$	$r_{\text{out}}$	$T(r_{\text{in}})$ ( $\times 10^{10}$ K)	$T(r_{\text{out}})$ ( $\times 10^{10}$ K)	Type
0 (Sch)	—	—	85.0892	—	0.2048	O
1	500	—	47.2185	—	0.3564	O
5	500	7.3900	—	1.7726	—	I
10	500	6.5138	—	2.1628	—	I
50	500	4.8793	—	4.6142	—	I
10	$10^5$	—	81.6338	—	0.2129	O
10	$10^4$	—	58.5248	—	0.2906	O
10	$10^3$	7.3628	—	1.7794	—	I
10	$10^2$	4.9843	—	4.4446	—	I

$\nu_o L_{\nu_o}$  and  $\nu_o$ , the slope ( $S$ ) of SED is calculated as,

$$S = \frac{d[\log(\nu_o L_{\nu_o})]}{d[\log(\nu_o)]}. \quad (30)$$

Using Eq. (30), we calculate the slope associated with the SEDs shown in Figs. 3a-b, and the obtained results are presented in Figs. 3c-d, respectively. It is observed that the SED slopes are nearly identical in the low to moderate frequency ranges. However, at high frequencies, they noticeably differ from each other. Additionally, from Figs. 3c-d, it is clearly seen that for the Schwarzschild BH and the Cardoso BH with low halo compactness, the SED slopes exhibit two plateau regions across the entire frequency range. In contrast, the SEDs for the Cardoso model with high compactness factors show only one plateau region. These spectral characteristics may provide valuable insights into the astrophysical observations for distinguishing a Schwarzschild BH from the Cardoso BH model. Note that the above findings are consistent with the work in [44], where the authors studied the spectral properties of accretion flows by treating the disc as a perfect black body emitter. In that study, the hydrodynamics of the flow were governed by the geodesic equation of the particles, with the flow reaching up to the innermost stable circular orbit. Furthermore, the flow velocity never surpasses the local sound speed, implying that the transonic accretion model was not considered. Thereafter, we calculate the bolometric luminosity ( $L$ ) of the accretion disc using Eq. (29) for the accretion solutions of Figs. 2a-b. The obtained results are depicted in panels (e) and (f) of Fig. 3, where the variation of  $L$  as a function of compactness parameter ( $C$ ) is shown. Here, the filled circles, using the same color codes as in Figs. 2a-b, joined by the dashed (gray) lines, denote the results for the re-

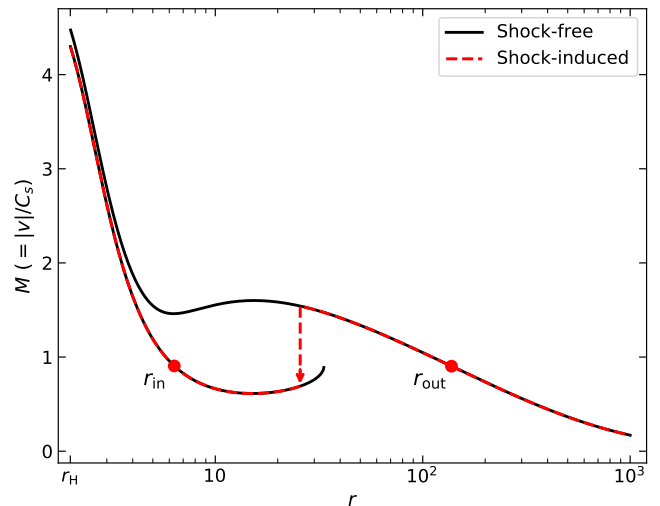


FIG. 4. Accretion solutions for the shock-free and shock-induced scenarios. The vertical line indicates the shock location ( $r_{\text{sh}}$ ) and the arrow represents the overall direction of the flow. In this figure, we choose  $\lambda = 3$ ,  $E = 1.0005$ ,  $M = 10$ , and  $a_0 = 10^4$ . See the text for details.

spective accretion solutions. In both panels, we notice that  $L$  increases with  $C$ . As the increase in  $M_{\text{H}}$  and  $a_0$  enhances the disc luminosity distribution (see Figs. 3a-b), it is therefore expected that the total disc luminosity also increases with halo compactness.

## B. Accretion with shocks

We previously mentioned that the flow can accommodate multiple critical points, depending on the input parameters. In this section, we illustrate such scenarios and analyze their characteristics in terms of shocks. Fig. 4 shows a typical solution topology with multiple critical points (solid black lines) for the set of global constants  $(\lambda, E, M_{\text{H}}, a_0) = (3, 1.0005, 10, 10^4)$ . The critical points are located at  $r_{\text{in}} = 6.3427$  and  $r_{\text{out}} = 137.617$ . It is observed that the solution passing through  $r_{\text{out}}$  is a global solution, while the solution passing through  $r_{\text{in}}$  is truncated at a radius  $r_t = 33.3527$ , referred to as a closed solution. Since closed solutions are not extended from  $r_{\text{H}}$  to  $r_{\text{edge}}$ , they are not considered physically acceptable. The entropy accretion rates ( $\dot{M}$ ) for the inner and outer branches are calculated to be  $4.2764 \times 10^7$  and  $3.3173 \times 10^7$ , respectively. Since the inner solution has a higher entropy content than the outer solution, the flow prefers to jump into the inner closed branch in the form of shocks, provided the relativistic shock conditions are satisfied. We calculate the shock location ( $r_{\text{sh}}$ ) using the

Rankine-Hugoniot standing shock conditions as [82],

$$[\rho u^r] = 0, \quad (31)$$

$$[(e + p)u^r u^t] = 0, \quad (32)$$

$$[(e + p)u^r u^r + pg^{rr}] = 0, \quad (33)$$

where the square brackets denote the difference of the quantities across  $r_{\text{sh}}$ . Eqs. (31), (32), and (33) correspond to the conservation of mass flux, energy flux, and radial-momentum flux across  $r_{\text{sh}}$ , respectively. The dashed (red) curve in Fig. 4 illustrates a shock-induced accretion solution, with a noticeable sharp jump at  $r_{\text{sh}} = 25.6527$ . Note that the shock solutions can pass through both  $r_{\text{in}}$  and  $r_{\text{out}}$  simultaneously.

We now explore various shock properties (e.g., shock radius, density compression, and temperature compression, etc.) in the presence of a dark matter halo and compare them with those for a Schwarzschild BH. In panels (a) and (b) of Fig. 5, we present the shock solutions for different values of halo mass  $M_{\text{H}}$  with a fixed length scale  $a_0 = 10^4$ , and for various values of  $a_0$  with  $M_{\text{H}} = 1$ . In this case, a given set of flow parameters is chosen as  $(\lambda, E) = (3, 1.00125)$ . Here, the solid (black) curves represent the result for the Schwarzschild BH. The dashed (red), dotted (blue), and dash-dotted (green) lines correspond to the Cardoso BH with  $M_{\text{H}} = 3, 6, \text{ and } 9$ , respectively. Similar color codes are used for  $a_0 = 10^4, 5 \times 10^3$ , and  $10^3$ , respectively. Using the shock conditions (31), (32), and (33), we obtain the shock locations at  $r_{\text{sh}} = 21.5735, 27.4824, 34.5320, \text{ and } 44.1920$  for  $M_{\text{H}} = 0, 3, 6, \text{ and } 9$ , respectively. On the other hand, for  $a_0 = 10^4, 5 \times 10^3$ , and  $10^3$ , the calculated shock locations are  $r_{\text{sh}} = 23.4964, 25.4094, \text{ and } 45.6867$ , respectively. The critical points and shock locations associated with these solutions are summarized in Table II. It is observed that the shock locations for the Schwarzschild BH are located closer to the horizon compared to those for the Cardoso BH. Furthermore, as the compactness of the halo increases, the shock fronts move away from the central object. For these shock solutions, the profiles of radial velocity ( $v$ ), mass density ( $\rho$ ), and electron temperature ( $T_e$ ) are presented in Figs. 5c-d, 5e-f, and 5g-h, respectively. It is observed that the analyzed flow variables undergo significant changes across the shock fronts. This occurs because, according to the shock condition (31), as  $v$  decreases at  $r_{\text{sh}}$ ,  $\rho$  increases. Also, due to the drop in  $v$ , kinetic energy of the flow is converted into thermal energy, resulting in an increase in  $T_e$  at  $r_{\text{sh}}$ . Moreover, we observe that the change in  $v$  at  $r_{\text{sh}}$  diminishes as the shock originates at larger radii, decreasing the difference of  $\rho$  and  $T_e$  across the shock fronts. We wish to mention that  $r_{\text{sh}}$  determines the size of the PSC, where a swarm of

TABLE II. Dark matter halo mass ( $M_{\text{H}}$ ), halo length scale ( $a_0$ ), critical point locations ( $r_{\text{in}}, r_{\text{out}}$ ), and shock location ( $r_{\text{sh}}$ ) for the shock solutions presented in Fig. 5.

$M_{\text{H}}$	$a_0$	$r_{\text{in}}$	$r_{\text{out}}$	$r_{\text{sh}}$
0 (Sch)	—	6.3435	159.9156	21.5735
3	$10^4$	6.3224	131.5024	27.4824
6	$10^4$	6.3020	110.6456	34.5320
9	$10^4$	6.2821	94.6018	44.1920
1	$10^4$	6.3364	149.3566	23.4964
1	$5 \times 10^3$	6.3294	140.5021	25.4094
1	$10^3$	6.2767	98.3629	45.6867

hot electrons can produce high-energy radiation through inverse Compton scattering. Such emissions are commonly observed in AGNs and BH-XRBs [4, 11, 83].

In this section, we also explore the luminosity spectrum of the accretion disc in the presence of shocks. For the shock-induced accretion solutions presented in Fig. 5a-b, we calculate their SEDs using Eq. (28). The results are shown in Fig. 6, where panel (a) and panel (b) correspond to the shock solutions in Figs. 5a-b, respectively. Similar to the Fig. 3, the radiation power maximizes at around  $\nu_o \approx 10^{20}$  Hz and cuts off at  $\nu_o \approx 10^{22}$  Hz. We see that for the shock scenario, the SEDs for the Schwarzschild BH case are negligibly higher than those for the Cardoso BH. Additionally, for the latter model, increasing  $M_{\text{H}}$  and  $a_0$  leads to a barely increase in the SEDs. The reason behind these observations is the negligible variations in the disc temperature profiles when the compactness of the dark matter halo is changed (see Figs. 5g-h). Moreover, the spectrum shape and the area under the SED (which effectively gives the bolometric luminosity  $L$ , see Eq. (29)) do not change significantly with variations in  $M_{\text{H}}$  and  $a_0$ .

### C. Shock parameter space

Here, we identify the effective region of the specific angular momentum ( $\lambda$ ) and energy ( $E$ ) that admits shock solutions for the Cardoso BH and compare it with that of the Schwarzschild BH. In Fig. 7a, we present the shock parameter space in the  $\lambda - E$  plane for different values of halo mass  $M_{\text{H}} = 5, 10, 15, \text{ and } 20$  with a fixed halo length scale of  $a_0 = 10^4$ . The regions bounded by the dashed (blue), dotted (red), dash-dotted (green), and long-dashed (magenta) curves represent the results for  $M_{\text{H}} = 5, 10, 15, \text{ and } 20$ , respectively. The parameter space enclosed by the solid (gray) line corresponds to the Schwarzschild BH model. We observe that for

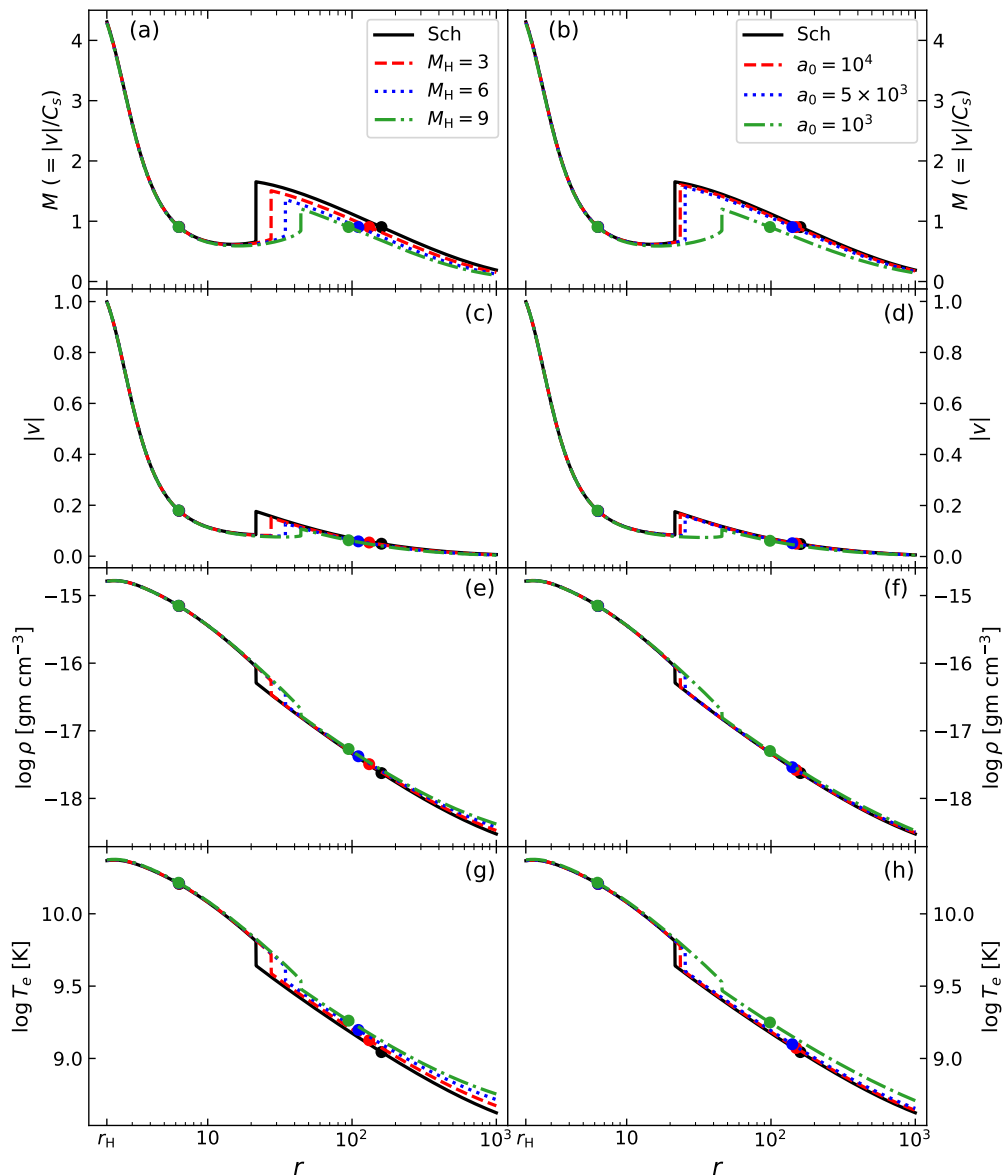


FIG. 5. Shock solutions for halo masses  $M_H = 3, 6,$  and  $9$  with length scale  $a_0 = 10^4$  (panel (a)), and for  $a_0 = 10^4, 5 \times 10^3,$  and  $10^3$  with  $M_H = 1$  (panel (b)). The corresponding radial velocity ( $v$ ), mass density ( $\rho$ ), and electron temperature ( $T_e$ ) profiles associated with these shock solutions are presented in panels (c)-(d), (e)-(f), and (g)-(h), respectively. In each panel, the shock locations are marked by vertical lines. In this figure, we set  $\lambda = 3$ ,  $E = 1.00125$ ,  $M_{\text{BH}} = 10^6 M_\odot$ , and  $\dot{M} = 10^{-5} \dot{M}_{\text{Edd}}$ . See the text for details.

the Schwarzschild BH, flow exhibits shocks at relatively higher  $\lambda$  and  $E$  values compared to the Cardoso BH. Also, the area under the shock parameter space is larger for the Schwarzschild BH than for the Cardoso BH. As  $M_H$  increases, the parameter space shifts toward lower  $\lambda$  and  $E$  domains, and the parameter space gradually shrinks as well. Similarly, in Fig. 7b, we present the modification of the shock parameter space in the  $\lambda - E$  plane for varying  $a_0$  with a fixed  $M_H = 1$ . The dashed (blue), dotted (red), dash-dotted (green), and long-dashed (magenta) curves

correspond to  $a_0 = 10^4, 5 \times 10^3, 10^3,$  and  $900$ , respectively. The shock parameter space for the Schwarzschild BH is bounded by the solid (gray) line. As in Fig. 7a, we find that the shock parameter space for the Schwarzschild BH without dark matter halo can accommodate higher  $\lambda$  and  $E$  values than in the presence of a halo. Additionally, the area under the parameter space decreases slightly when  $a_0$  decreases from  $10^4$  to  $5 \times 10^3$ . However, the parameter space shrinks significantly when  $a_0$  decreases further to smaller values, such as  $10^3$  and  $900$ .

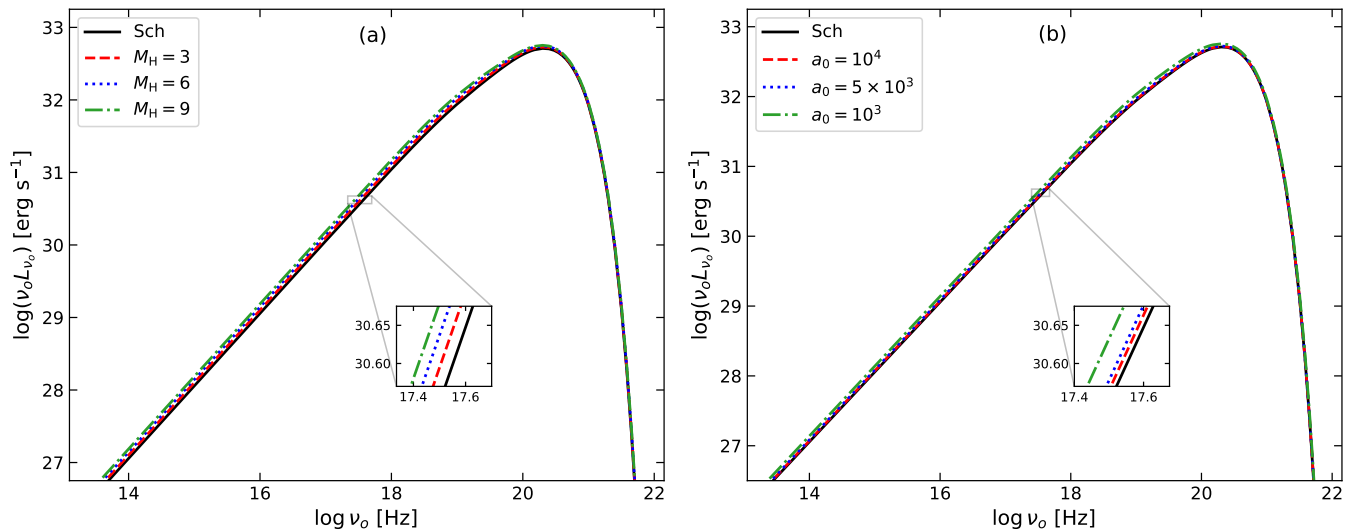


FIG. 6. Spectral energy distributions of the accretion disc for shock-induced flow solutions presented in Figs. 5a-b. In this figure, we choose the set of the input parameters as  $r_{\text{edge}} = 1000$ ,  $\lambda = 3$ ,  $E = 1.00125$ ,  $M = 10^6 M_{\odot}$ , and  $\dot{M} = 10^{-5} \dot{M}_{\text{Edd}}$ . See the text for details.

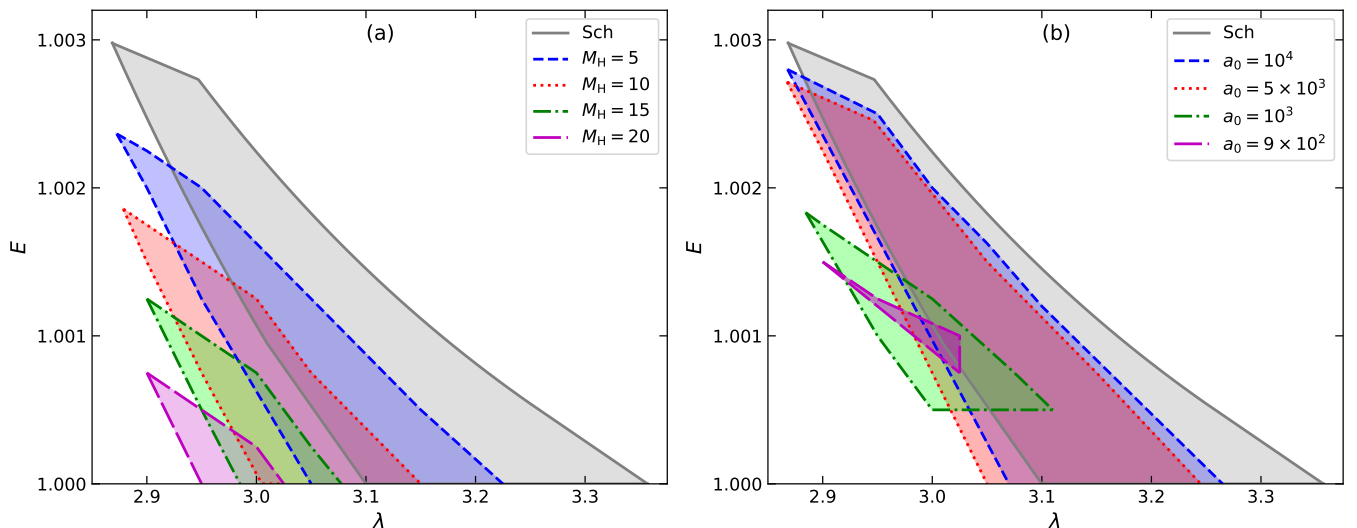


FIG. 7. Modification of the shock parameter space in specific angular momentum ( $\lambda$ ) and energy ( $E$ ) plane for the halo masses  $M_H = 5, 10, 15$ , and  $20$  with  $a_0 = 10^4$  (panel (a)), and for  $a_0 = 10^4, 5 \times 10^3, 10^3$ , and  $900$  with  $M_H = 1$  (panel (b)). In each panel, the effective region within the gray (solid) line corresponds to the Schwarzschild BH without a dark matter halo (i.e.,  $M_H = 0$ ). See the text for details.

## V. CONCLUSION AND DISCUSSION

In this work, we explore the transonic accretion flow around a galactic black hole with a dark matter halo, as proposed in [21]. The flow hydrodynamics in the accretion disc are modeled within fully general relativistic framework. Using the relativistic equation of state, we numerically solve the radial momentum and energy equations. Consequently, we obtain the global accretion so-

lutions in both the presence and absence of shocks. As the halo compactness primarily influences the dynamics of the accretion flow through the effective potential ( $\Phi^{\text{eff}}$ ) of the system, the main objective of this work is to explore the effect of halo mass ( $M_H$ ) and length scale ( $a_0$ ) on the physical properties of the accretion disc. We make an effort to compare these results with those for the usual Schwarzschild BH without a dark matter halo. We summarize our findings point-wise below.

- We find O-type and I-type accretion solutions, where the flow possesses single critical points either far from the horizon (O-type) or near the horizon (I-type). We observe that for the Schwarzschild BH and the Cardoso BH with small halo compactness, the solution topology remains O-type. However, at higher values of  $M_{\text{H}}$  and  $a_0$ , the solution topology changes to I-type.
- We also obtain A-type multiple critical point solutions and observe that such solutions can admit standing shock transitions when the flow satisfies the relativistic shock conditions. It is noticed that the shock solutions are not unique but rather exist within a broad range of the parameter space spanned by the flow specific angular momentum ( $\lambda$ ) and energy ( $E$ ). Accordingly, we examine the modification of the shock parameter space as a function of  $M_{\text{H}}$  and  $a_0$ . We observe that the shock parameter space is larger for the Schwarzschild BH compared to the Cardoso BH. However, a small increase in the halo compactness significantly shrinks the shock parameter space. This result suggests that the shock solutions exist in an extremely small  $\lambda - E$  parameter space for a high value of compactness parameter  $C$  ( $= M_{\text{H}}/a_0 \gtrsim 0.001$ ).
- Furthermore, we examine the effect of  $M_{\text{H}}$  and  $a_0$  on various shock properties, particularly the shock location ( $r_{\text{sh}}$ ), as well as the changes in mass density ( $\rho$ ) and electron temperature ( $T_e$ ) across the standing shocks. We find that the shock fronts settle down at smaller radii for the Schwarzschild BH than the Cardoso BH. Moreover, as  $M_{\text{H}}$  and  $a_0$  increase,  $r_{\text{sh}}$  moves away from the horizon, leading to a decrease in the changes of  $\rho$  and  $T_e$  across  $r_{\text{sh}}$ .
- In addition, we calculate the spectral energy distribution (SED) for both the shock-free and shock-induced accretion solutions using the relativistic thermal bremsstrahlung emission coefficient. For the shock-free scenario, SEDs significantly increase with the rise in  $M_{\text{H}}$  and  $a_0$ . This outcome agrees with existing work in the literature based on a different accretion model [44]. While investigating the SED slope ( $S$ ), we observe that  $S$  possesses two plateau regions across the entire frequency domain for both the Schwarzschild BH and the Cardoso BH with small halo compactness. As the compactness parameters increase to moderate values, the profile of  $S$  starts differing noticeably at high-frequency domains. For very high halo compactness, only

one plateau region remains in the low to moderate frequency range. As the luminosity distributions potentially increase with  $M_{\text{H}}$  and  $a_0$ , the bolometric disc luminosity ( $L$ ) also increases with the halo compactness. On the other hand, for shock solutions, the SEDs barely change with  $M_{\text{H}}$  and  $a_0$ , resulting in insignificant variations in both  $S$  and  $L$  with the compactness parameter. Therefore, alongside the quantitative variabilities, the change in the spectrum shape provides a clear distinction between the Cardoso BH and Schwarzschild BH models.

In conclude, the present study indicates that the dark matter halo significantly influences the dynamical and spectral characteristics of the accretion flow around a galactic black hole when it is concentrated close to the black hole. However, the transonic accretion properties of such black hole geometry give nearly identical results as those around vacuum Schwarzschild BHs when the compactness does not exceed the limit given by the galaxy observation ( $C \lesssim 10^{-4}$ ). This identification is similar to the observations in [84] regarding the geodesic motion of the orbiting particles.

Finally, we highlight the limitations of our work. In our model, the angular momentum is a conserved quantity due to the assumption of ideal fluid dynamics. However, the viscous stress can transport angular momentum towards the outer edge of the disc [66, 70, 85]. Additionally, our accretion model does not account for magnetic fields. But, the presence of large-scale magnetic fields can alter the dynamics of the accreting material through the magnetic pressure [62, 65]. We also do not incorporate the synchrotron and Comptonization emission processes [86, 87]. Moreover, due to the high temperature gradient near the inner regions of the disc, thermal conduction plays an important role in influencing the behavior of the accretion disc [88, 89]. However, the present study has neglected the thermal conduction mechanism. Furthermore, we adopt a simple scaling relation between the electron and ion temperatures, although several studies in the literature have explored two-temperature accretion flows [87, 90–93]. It is important to note that these physical processes are highly relevant in the context of black hole accretion flows. We plan to address these aspects in future work and report the outcomes elsewhere.

#### DATA AVAILABILITY STATEMENT

The data underlying this article will be available with reasonable request.



## ACKNOWLEDGMENTS

The authors would like to thank Chiranjeeb Singha and Soumya Bhattacharya for useful discussions. SP acknowledges the University Grants Commission (UGC),

India, for the financial support through the Senior Research Fellowship (SRF) scheme. The work of BRM is supported by a START-UP RESEARCH GRANT from the Indian Institute of Technology Guwahati (IIT Guwahati), India, under the grant SG/PHY/P/BRM/01.

- 
- [1] J. E. Pringle, Annual review of astronomy and astrophysics **19**, 137 (1981).
- [2] J. Frank, A. King, and D. Raine, *Accretion power in astrophysics* (Cambridge university press, 2002).
- [3] A. A. Esin, R. Narayan, W. Cui, J. E. Grove, and S.-N. Zhang, The Astrophysical Journal **505**, 854 (1998).
- [4] A. Nandi, S. Das, S. Majumder, T. Katoch, H. M. Antia, and P. Shah, Mon. Not. Roy. Astron. Soc. **531**, 1149 (2024), 2404.17160.
- [5] M. A. Abramowicz and P. C. Fragile, Living Reviews in Relativity **16**, 1 (2013).
- [6] F. Yuan and R. Narayan, Ann. Rev. Astron. Astrophys. **52**, 529 (2014), 1401.0586.
- [7] A. Nandi, S. Mandal, H. Sreehari, D. Radhika, S. Das, I. Chattopadhyay, N. Iyer, V. Agrawal, and R. Aktar, Astrophysics and Space Science **363**, 1 (2018).
- [8] H. Sreehari, A. Nandi, S. Das, V. Agrawal, S. Mandal, M. Ramadevi, and T. Katoch, Monthly Notices of the Royal Astronomical Society **499**, 5891 (2020).
- [9] S. Das, A. Nandi, V. K. Agrawal, I. K. Dihingia, and S. Majumder, Mon. Not. Roy. Astron. Soc. **507**, 2777 (2021), 2108.02973.
- [10] K. Sriram, S. Harikrishna, and C. S. Choi, Astrophys. J. **911**, 127 (2021), 2103.02422.
- [11] S. Majumder, S. H., N. Aftab, T. Katoch, S. Das, and A. Nandi, Mon. Not. Roy. Astron. Soc. **512**, 2508 (2022), 2203.02710.
- [12] S. Mondal, T. P. Adhikari, K. Hryniewicz, C. Stalin, and A. Pandey, Astronomy & Astrophysics **662**, A77 (2022).
- [13] S. R. Heiland, A. Chatterjee, S. Safi-Harb, A. Jana, and J. Heyl, Mon. Not. Roy. Astron. Soc. **524**, 3834 (2023), 2307.06395.
- [14] D. Rawat, M. Méndez, F. García, D. Altamirano, K. Karpouzas, L. Zhang, K. Alabarta, T. M. Belloni, P. Jain, and C. Bellavita, Mon. Not. Roy. Astron. Soc. **520**, 113 (2023), 2301.04418.
- [15] R. Dhaka, R. Misra, J. S. Yadav, and P. Jain, Mon. Not. Roy. Astron. Soc. **524**, 2721 (2023), 2307.04622.
- [16] S. Mondal, M. Das, K. Rubinur, K. Bansal, A. Nath, and G. B. Taylor, Astron. Astrophys. **691**, A279 (2024), 2409.05717.
- [17] A. A. Molla, S. K. Chakrabarti, D. Debnath, and S. Mondal, Astrophys. J. **834**, 88 (2017), 1611.01266.
- [18] S. Mondal, S. P. Suribhatla, K. Chatterjee, C. B. Singh, and R. Chatterjee, Astrophys. J. **975**, 257 (2024), 2404.09643.
- [19] L. Sadeghian, F. Ferrer, and C. M. Will, Phys. Rev. D **88**, 063522 (2013), 1305.2619.
- [20] G. Bertone and T. M. Tait, Nature **562**, 51 (2018).
- [21] V. Cardoso, K. Destounis, F. Duque, R. P. Macedo, and A. Maselli, Phys. Rev. D **105**, L061501 (2022), 2109.00005.
- [22] I. King, Astron. J. **67**, 471 (1962).
- [23] J. Einasto, Trudy Astrofizicheskogo Instituta Alma-Ata, Vol. 5, p. 87-100, 1965 **5**, 87 (1965).
- [24] W. Jaffe, Monthly Notices of the Royal Astronomical Society **202**, 995 (1983).
- [25] A. Burkert, The Astrophysical Journal **447**, L25 (1995).
- [26] J. F. Navarro, C. S. Frenk, and S. D. M. White, Astrophys. J. **462**, 563 (1996), astro-ph/9508025.
- [27] B. Moore, T. R. Quinn, F. Governato, J. Stadel, and G. Lake, Mon. Not. Roy. Astron. Soc. **310**, 1147 (1999), astro-ph/9903164.
- [28] A. Di Cintio, C. B. Brook, A. A. Dutton, A. V. Macciò, G. S. Stinson, and A. Knebe, Mon. Not. Roy. Astron. Soc. **441**, 2986 (2014), 1404.5959.
- [29] Z. Xu, X. Hou, X. Gong, and J. Wang, JCAP **09**, 038 (2018), 1803.00767.
- [30] R. A. Konoplya and A. Zhidenko, Astrophys. J. **933**, 166 (2022), 2202.02205.
- [31] K. Jusufi, Eur. Phys. J. C **83**, 103 (2023), 2202.00010.
- [32] V. De Luca and J. Khoury, JCAP **04**, 048 (2023), 2302.10286.
- [33] R. Acharyya, P. Banerjee, and S. Kar, JCAP **04**, 070 (2024), 2311.18622.
- [34] D. Liu, Y. Yang, and Z.-W. Long, Eur. Phys. J. C **84**, 731 (2024), 2401.09182.
- [35] R. Bécar, P. A. González, E. Papantonopoulos, and Y. Vásquez, JCAP **06**, 061 (2024), 2403.11306.
- [36] M. M. Gohain, P. Phukon, and K. Bhuyan, Phys. Dark Univ. **46**, 101683 (2024), 2407.02872.
- [37] E. Retana-Montenegro, E. van Hese, G. Gentile, M. Baes, and F. Frutos-Alfaro, Astronomy and Astrophysics **540**, A70 (2012), 1202.5242.
- [38] K. Jusufi, M. Jamil, and T. Zhu, Eur. Phys. J. C **80**, 354 (2020), 2005.05299.
- [39] T. Igata, T. Harada, H. Saida, and Y. Takamori, Int. J. Mod. Phys. D **32**, 2350105 (2023), 2202.00202.
- [40] N. Dai, Y. Gong, Y. Zhao, and T. Jiang, Phys. Rev. D **110**, 084080 (2024), 2301.05088.
- [41] S. V. M. C. B. Xavier, H. C. D. Lima, Junior., and L. C. B. Crispino, Phys. Rev. D **107**, 064040 (2023), 2303.17666.

- [42] Y. S. Myung (2024), 2402.03606.
- [43] S. Kazempour, S. Sun, and C. Yu, *Phys. Rev. D* **110**, 043034 (2024), 2404.11333.
- [44] M. Heydari-Fard, M. Heydari-Fard, and N. Riazi (2024), 2408.16020.
- [45] R.-Y. Chen, F. Javed, D. G. Mustafa, S. K. Maurya, and S. Ray, *JHEAp* **44**, 172 (2024).
- [46] Q. Tan, W. Deng, S. Long, and J. Jing (2024), 2409.17760.
- [47] Y. Zhao, N. Dai, and Y. Gong (2024), 2410.06882.
- [48] A. Mollicone and K. Destounis, *Phys. Rev. D* **111**, 024017 (2025), 2410.11952.
- [49] L. Pezzella, K. Destounis, A. Maselli, and V. Cardoso (2024), 2412.18651.
- [50] T. S. Amancio, R. A. Mosna, and R. S. S. Vieira, *Phys. Rev. D* **110**, 124048 (2024), 2412.15938.
- [51] E. Liang and K. Thompson, *The Astrophysical Journal* **240**, 271 (1980).
- [52] M. A. Abramowicz and W. Zurek, *The Astrophysical Journal* **246**, 314 (1981).
- [53] J. Fukue, *Publications of the astronomical society of Japan* **39**, 309 (1987).
- [54] R. A. Konoplya, *Phys. Lett. B* **823**, 136734 (2021), 2109.01640.
- [55] Z. Stuchlík and J. Vrba, *JCAP* **11**, 059 (2021), 2110.07411.
- [56] J. Liu, S. Chen, and J. Jing, *Chin. Phys. C* **46**, 105104 (2022), 2203.14039.
- [57] S. K. Chakrabarti, *Mon. Not. Roy. Astron. Soc.* **283**, 325 (1996), astro-ph/9611019.
- [58] R. Kumar and I. Chattopadhyay, *Monthly Notices of the Royal Astronomical Society* **469**, 4221 (2017).
- [59] I. K. Dihingia, S. Das, D. Maity, and S. Chakrabarti, *Physical Review D* **98**, 083004 (2018).
- [60] I. K. Dihingia, D. Maity, S. Chakrabarti, and S. Das, *Physical Review D* **102**, 023012 (2020).
- [61] S. Patra, B. R. Majhi, and S. Das, *Phys. Dark Univ.* **37**, 101120 (2022), 2202.10863.
- [62] S. Mitra, D. Maity, I. K. Dihingia, and S. Das, *Mon. Not. Roy. Astron. Soc.* **516**, 5092 (2022), 2204.01412.
- [63] G. Sen, D. Maity, and S. Das, *JCAP* **08**, 048 (2022), 2204.02110.
- [64] S. Patra, B. R. Majhi, and S. Das, *JCAP* **01**, 060 (2024), 2308.12839.
- [65] S. Mitra and S. Das, *Astrophys. J.* **971**, 28 (2024), 2405.16326.
- [66] S. Patra, B. R. Majhi, and S. Das, *JHEAp* **44**, 371 (2024), 2407.07968.
- [67] S. Patra, B. R. Majhi, and S. Das (2024), 2412.17108.
- [68] R. Aktar, S. Das, A. Nandi, and H. Sreehari, *J. Astrophys. Astron.* **39**, 17 (2018), 1801.04116.
- [69] S. Das, A. Nandi, C. S. Stalin, S. Rakshit, I. K. Dihingia, S. Singh, R. Aktar, and S. Mitra, *Mon. Not. Roy. Astron. Soc.* **514**, 1940 (2022), 2205.07737.
- [70] I. Dihingia, S. Das, D. Maity, and A. Nandi, *Mon. Not. Roy. Astron. Soc.* **488**, 2412 (2019), 1903.02856.
- [71] L. Rezzolla and O. Zanotti, *Relativistic Hydrodynamics* (Oxford University Press, 2013), ISBN 978-0-19-174650-5, 978-0-19-852890-6.
- [72] J. Lasota, in *Theory of Accretion Disks—2: Proceedings of the NATO Advanced Research Workshop on Theory of Accretion Disks—2 Garching, Germany March 22–26, 1993* (Springer, 1994), pp. 341–349.
- [73] H. Riffert and H. Herold, *Astrophysical Journal* v. 450, p. 508 **450**, 508 (1995).
- [74] J. Peitz and S. Appl, *Mon. Not. Roy. Astron. Soc.* **286**, 681 (1997), astro-ph/9612205.
- [75] I. Chattopadhyay and D. Ryu, *The Astrophysical Journal* **694**, 492 (2009).
- [76] R. Yarza, G. N. Wong, B. R. Ryan, and C. F. Gammie, *Astrophys. J.* **898**, 50 (2020), 2006.01145.
- [77] I. Chattopadhyay and R. Kumar, *Mon. Not. Roy. Astron. Soc.* **459**, 3792 (2016), 1605.00752.
- [78] I. D. Novikov and K. S. Thorne, *Black holes (Les astres occlus)* **1**, 343 (1973).
- [79] J.-P. Luminet, *Astronomy and Astrophysics* **75**, 228 (1979).
- [80] G. B. Rybicki and A. P. Lightman, *Radiative processes in astrophysics* (John Wiley & Sons, 1991).
- [81] S. K. Chakrabarti, *Astrophys. J.* **347**, 365 (1989).
- [82] A. H. Taub, *Phys. Rev.* **74**, 328 (1948).
- [83] K. Chatterjee, S. Mondal, C. B. Singh, and M. Sugizaki, *Astrophys. J.* **977**, 148 (2024), 2405.01498.
- [84] K. Destounis, A. Kulathingal, K. D. Kokkotas, and G. O. Papadopoulos, *Phys. Rev. D* **107**, 084027 (2023), 2210.09357.
- [85] M. Singh and S. Das, *Astrophys. Space Sci.* **369**, 1 (2024), 2312.16001.
- [86] I. K. Dihingia, S. Das, G. Prabhakar, and S. Mandal, *Mon. Not. Roy. Astron. Soc.* **496**, 3043 (2020), 1911.02757.
- [87] S. Sarkar and I. Chattopadhyay, *Journal of Astrophysics and Astronomy* **43**, 34 (2022).
- [88] S. Mitra, S. M. Ghoreyshi, A. Mosallanezhad, S. Abbassi, and S. Das, *Mon. Not. Roy. Astron. Soc.* **523**, 4431 (2023), 2306.02453.
- [89] M. Singh and S. Das (2024), 2408.02256.
- [90] S. Sarkar and I. Chattopadhyay, *Int. J. Mod. Phys. D* **28**, 1950037 (2018), 1811.05947.
- [91] I. K. Dihingia, S. Das, and S. Mandal, *Journal of Astrophysics and Astronomy* **39**, 1 (2018).
- [92] I. K. Dihingia, S. Das, G. Prabhakar, and S. Mandal, *Monthly Notices of the Royal Astronomical Society* **496**, 3043 (2020).
- [93] S. Sarkar, I. Chattopadhyay, and P. Laurent, *Astronomy & Astrophysics* **642**, A209 (2020).